Journal of Information Systems Engineering and Management
2025, 10(21s)
e-ISSN: 2468-4376
https://www.jisem-journal.com/

Research Article

Identification and Detection of Ferroresonance Phenomenon in Active Distribution Networks Using Long Short-Term Memory Neural Networks Enhanced by Genetic Algorithm

Anita Ershadi Oskouei[1], Ali Vaziri[2], Pardis Sadatian Moghaddam[3]

[1]Department of Systems and Enterprises, Stevens Institute of Technology, Hoboken, NJ 07030, USA. (Corresponding Author)aershadi@stevens.edu

[2]Department of Systems and Enterprises, Stevens Institute of Technology, Hoboken, NJ 07030, USA. avaziri1@stevens.edu

[3]Department of Computer Science, Georgia State University, Atlanta, Georgia.psadatian1@student.gsu.edu

ARTICLE INFO

Received: 22 Dec 2024

Revised: 31 Jan 2025

Accepted: 15 Feb 2025

ABSTRACT

Given the importance of detecting the ferroresonance phenomenon and distinguishing it from other transient events in active distribution networks, this paper proposes the use of Long Short-Term Memory (LSTM) recurrent neural networks to achieve this goal. In the proposed LSTM network, the optimization of learning period parameters, hidden layers, and corresponding weight coefficients is performed using a Genetic Algorithm (GA) to enhance the detection accuracy and speed. To create a suitable time-sequence database for LSTM training, an active distribution network comprising wind turbines, photovoltaic systems, and synchronous diesel generators is modeled in PSCAD software. By simulating various transient events, such as phase disconnections, capacitor bank switching, and load switching, the calculated detail and approximation coefficients up to six levels of the three-phase voltage waveforms of feeders are used as input features during the LSTM network training phase. Subsequently, to validate and confirm the effectiveness of the proposed LSTM-GA model, numerical studies are conducted on this active distribution network for the identification and distinction of the ferroresonance phenomenon. Simulation results confirm that optimizing and tuning the LSTM network parameters with GA significantly improves performance metrics, including precision, accuracy (P), recall (R), and others.

Keywords: Ferroresonance phenomenon, Long Short-Term Memory (LSTM) recurrent neural network, learning period and hidden layers, database, active distribution network, Genetic Algorithm.

INTRODUCTION

One of the primary challenges in power quality, particularly in active distribution networks, is the occurrence of the ferroresonance phenomenon. The overvoltage and overcurrent caused by this phenomenon can lead to the overheating and failure of measurement and power transformers. The characteristics of ferroresonance, including voltage and frequency oscillations, vary depending on initial conditions, excitation voltage and frequency, and circuit parameters such as capacitance and the magnetic core's saturation curve. Due to the critical importance of identifying and diagnosing ferroresonance, numerous studies have been conducted in this area. For instance, in [1], a multilayer perceptron was employed to detect this phenomenon in distribution networks, achieving 93% accuracy in classifying transformer switching and load switching signals. In [2], artificial neural networks were used to classify overvoltage oscillations caused by ferroresonance in power transformers, achieving an accuracy of 75.98%. In [3], a wavelet-based predictive neural network model was proposed to differentiate capacitor switching from ferroresonance, with an accuracy of 97%. In [4], the capability of wavelet-based neural networks to detect ferroresonance was analyzed, and in [5], this approach achieved 94% accuracy. In [6], ferroresonance classification was performed using a smart tracking and suppression system based on fuzzy logic, evaluating eight different events and achieving 100% accuracy. In [7], a Kalman filter was proposed for analyzing and detecting voltage waveform and amplitude during chaotic ferroresonance. In [8], transformer voltage oscillations were used to identify ferroresonance. In [9], a decentralized autoencoder classifier achieved 97% accuracy in ferroresonance detection. Finally, in [10], a study focused on electromagnetic transients with ferroresonance characteristics and introduced key parameters influencing its occurrence in power systems.

A review of recent studies reveals that, despite the high capability of Long Short-Term Memory (LSTM) networks in predicting sequential events, they have not yet been applied for estimating ferroresonance in active distribution

networks. Therefore, this paper aims to address this gap. The remainder of the paper is organized as follows. Section 2 introduces the wavelet transform as a feature extraction tool, including approximation and detail coefficients at various levels, and presents the LSTM recurrent neural network as a supervised classification tool for sequential data. Section 3 provides the mathematical formulation of performance evaluation metrics. Section 4 outlines the proposed flowchart for combining LSTM with a Genetic Algorithm (GA) to achieve accurate and rapid detection of ferroresonance based on input features derived from voltage waveforms. Section 5 presents numerical studies on a test active distribution network to validate and confirm the proposed method's performance, with metrics including accuracy, precision, recall, and F1 score. Finally, Section 6 discusses the conceptual results obtained from the case studies.

2. WAVELET TRANSFORM AND LSTM RECURRENT NEURAL NETWORK

2.1 Wavelet Transform

Today, wavelet transform is considered an advanced tool for time-frequency analysis of signals corresponding to various physical phenomena. It allows the decomposition of a signal into different frequencies with varying resolutions. Specifically, the wavelet transform provides good temporal resolution and poor frequency resolution at high frequencies, while at low frequencies, it offers good frequency resolution and poor temporal resolution. When the wavelet transform is applied to a spectral component, the window length varies, which is arguably the most important feature of wavelet transform. The continuous wavelet transform is modeled using equations (1) and (2):

$$C(a,b) = \int_{-\infty}^{+\infty} f(t)\psi_{a,b}(t)dt \quad (1)$$

$$\psi_{a,b}(t) = a^{\frac{-1}{2}}\psi_{a,b}\left(\frac{t-b}{a}\right) \quad (2)$$

Here, $\psi_{a,b}(t)$ is the mother wavelet, and a and b are the scale and translation coefficients, respectively. The term "wavelet" implies "small wave," where "small" refers to a finite-length window function, and "wave" refers to its oscillatory nature. The term "mother" indicates that functions with different functional regions used in the transform are derived from a single main or mother function.The term "translation" refers to the shifting of the window along the signal, which relates to temporal information in the transform domain. Additionally, "scaling" refers to the mathematical transformation that compresses or stretches the signal. Smaller scales correspond to expanded signals, while larger scales correspond to compressed signals. In wavelet transform, the scaling parameter is used in the denominator, meaning the inverse relationship holds—low scales correspond to high frequencies, and high scales correspond to low frequencies.

There are three main types of wavelet transform: continuous, semi-discrete, and discrete, differing in how scaling and shifting are implemented. For signals with limited energy, a suitable wavelet transform can allow reconstruction of the original signal without requiring all decomposition values. In such cases, the discrete wavelet transform (DWT) is sufficient, rendering continuous analysis unnecessary.

In the DWT, the scale and translation parameters of the mother wavelet are calculated using equations (3) and (4). Here, aaa and bbb are real positive numbers, a>1a > 1a>1, and b>0b > 0b>0, while mmm and nnn are positive integers. Consequently, the mother wavelet can be rewritten as in equation (5), and the corresponding DWT relation is computed using equation (6). The DWT decomposes a signal into multiple sub-bands, where the bandwidth increases linearly with frequency.

The implementation of DWT filter banks (Mallat's algorithm) involves sequential filtering of the signal using low-pass and high-pass filters, followed by subsampling, as shown in Figure 1. The initial signal can be reconstructed, as shown in Figure 2, through wavelet series reconstruction according to equation (7). Wavelet coefficients are obtained using inner products as per equation (8) [4]-[5].

$$a = a_0^m \quad (3)$$

$$b = n.b_0.a_0^m \quad (4)$$

$$\psi_{m,n}(t) = \frac{1}{\sqrt{a_0^m}} \psi_{a,b}\left(\frac{t - n.b_0.a_0^m}{a_0^m}\right) \tag{5}$$

$$DWT_{\Psi}.f(m,n) = \sum_{K} f(K).\psi_{m,n}(K) \tag{6}$$

$$f = \sum_{m}\sum_{n} C_{m,n}.\psi_{m,n} \tag{7}$$

$$C_{m,n} = \langle f.\tilde{\psi}_{m,n} \rangle \tag{8}$$

Figure 1: Mallat's Algorithm for Signal Decomposition Using Wavelet Transform

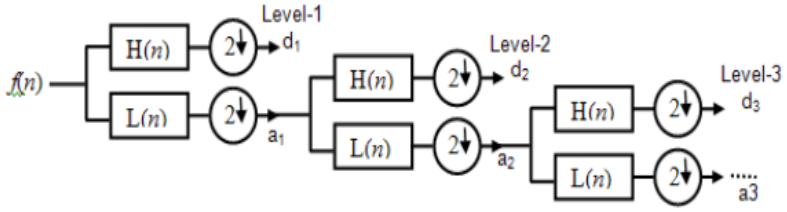

Figure 2: Mallat Tree Algorithm for Signal Reconstruction

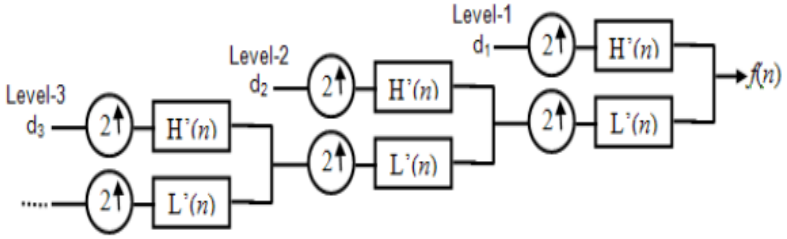

2.2 Long Short-Term Memory (LSTM)

Recurrent neural networks (RNNs) have many applications but also face challenges. One of their main problems is the vanishing gradient issue during learning from data with long temporal sequences, which reduces their learning ability. If the number of layers in the neural network increases, the backpropagation process does not function correctly, leading to gradient decay. This vanishing also occurs when the number of sequences in RNNs increases.

LSTM neural networks are a type of RNN that have modified block structures to manage long-term memory and eliminate the vanishing or exploding gradient problem. Compared to a simple RNN block, as shown in Figure (3), the LSTM block has a different structure. Unlike the simple RNN, which had two inputs (x and h), this structure has three inputs: x, h, and ccc, where x is the input at time (sequence) t, and h, like in a simple RNN, is the "hidden state" that receives the output from the previous time (previous sequence) as memory. The ccc input is a "cell state" that regulates how much information from past long sequences and which parts of it influence the current block [12].

For better understanding, the LSTM block can be divided into three main parts. The first part of this block, as shown in Figure (4), is called the "forget gate," which decides which part of the long-term information from the previous block is useful and which part is not. In this section, the "current input" (x) and "previous hidden state" (h) are combined with weights and passed through the sigmoid activation function. The output is then multiplied by the "cell state" (c). In this section, learning is done by the weights of a small internal neural network, combining x and h to regulate ccc.

In the second part of this block, as shown in Figure (5), it is decided what new information should be added to the "cell state" (c) for future use. This part is called the "input gate," which is formed by combining the "current input" (x) and the "previous hidden state" (h) with the weights of small internal neural networks and the output of the forget gate.

The third part of this block, as shown in Figure (6), is called the "output gate," which determines the outputs based on a combination of the updated "cell state" (ccc), the "current input" (x), and the "previous hidden state" (h). In this section, an internal neural network is also used for learning, and the outputs h and ccc are used in the next time step (t+1), i.e., the next sequence, in the same manner [11].

Figure 3: Inside a Long Short-Term Memory (LSTM) block [11]

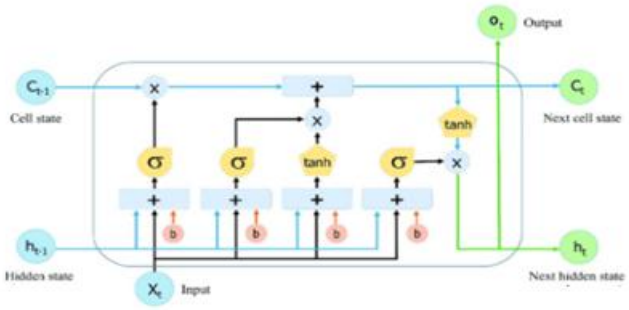

Intuitively, the cell state (c) added in LSTM compared to the simple RNN acts as a "highway," allowing information to pass through the network (across sequences) without interference from more complex elements, thus preventing the vanishing gradient problem. To express the mathematical relationships in the LSTM neural network, consider Figure (7). If x_t refers to the current input vector, the indices ct and ct−1 refer to the current and previous cell states, and the indices ht and ht−1 refer to the current and previous outputs, then the relationships are defined by Equations (9) to (10).

$$i_t = \sigma(W_i.[h_{t-1}, x_t] + b_i) \quad (9)$$

$$\tilde{C}_t = \tanh(W_i.[h_{t-1}, x_t] + b_i) \quad (10)$$

$$C_t = f_t C_{t-1} + i_t \tilde{C}_t \quad (11)$$

$$f_t = \sigma(W_f.[h_{t-1}, x_t] + b_f) \quad (12)$$

$$O_t = \sigma(W_O.[h_{t-1}, x_t] + b_O) \quad (13)$$

$$h_t = O_t \tanh(C_t) \quad (14)$$

Figure 7: Structure of the LSTM Recurrent Neural Network [11]

Equation (9) is used for passing x_t h_{t-1} through a sigmoid layer to decide which part of the information should be added. Equation (10) provides new information after passing x_t and h_{t-1} through a tanh layer. The indices Wiand bi refer to the weight matrices and biases of the input gate, respectively.

The current information xt and long-term memory c_{t-1} are combined in ct , as shown in Equation (11), where ft refers to the output of the sigmoid function and $\tilde{C}_t$ refers to the output of the tanh function.

Decisions about forgetting parts of previous cell states are made using Equation (12). Here, W_f refers to the weight matrix, b_f refers to the offset, and σ is the sigmoid function.

The LSTM output gate determines which states should be continued using the inputs x_t and h_{t-1}, as given in Equations (13) and (14). The final output is provided by multiplying the decision vector C_t with the new information vector using a tanh layer. The indices bo refer to the weight matrix and bias of the output gate, respectively.

3. Common Performance Evaluation Metrics

The performance of the Long Short-Term Memory (LSTM) recurrent neural network for classifying the status of the distribution network—whether it is experiencing the ferroresonance phenomenon or not—can be evaluated using

several common metrics. These metrics include the accuracy of the classifier, computational complexity during training and classification, sensitivity to noisy data, scalability, and so on.

To evaluate the performance of the ferroresonance classifier in the distribution network, the following definitions are considered:

- True Positive (TP): Refers to the number of records belonging to class A that are correctly predicted as class A.
- False Positive (FP): Refers to the number of records that do not belong to class A but are incorrectly classified as class A.
- True Negative (TN): Refers to the number of records that do not belong to class AAA and are correctly classified outside of class A.
- False Negative (FN): Refers to the number of records belonging to class A but are incorrectly predicted as not belonging to class A.

These metrics, in addition to evaluating the network status in class A, can also be calculated for network statuses in classes B and C from the dataset.

One of the most common performance evaluation metrics is accuracy, defined as the fraction of all correctly classified records out of the total records, as shown in Equation (15). However, using accuracy as a metric is not always appropriate in certain cases. In practical real-world classification problems, various types of errors may occur, and each type may incur different costs.

Other common metrics include precision (P) and recall (R), which are calculated using Equations (16) and (17), respectively:

- Precision (P): Indicates the percentage of times a record predicted as class AAA actually belongs to class A.
- Recall (R): Indicates how well the classifier can correctly identify all records belonging to class A.

It is important to note that both precision and recall have their own limitations. For example, predicting all records as class A would maximize recall but significantly reduce precision.

To address this issue, another metric called the F1 score is introduced, which combines precision and recall into a single metric, as shown in Equation (18). The F1 score balances precision and recall, providing a more comprehensive evaluation of the classifier's performance.

$$Accuracy = (TP+TN) \Big/ (TP+TN+FP+FN) \tag{15}$$

$$P = \frac{TP}{TP+FP} \tag{16}$$

$$R = \frac{TP}{TP+FN} \tag{17}$$

$$F_1 = \frac{2RP}{R+P} = \frac{2TP}{2TP+FN+FP} \tag{18}$$

A key factor affecting model performance is the distribution of classes and the size of the training and testing sets.To illustrate the impact of training set size, a learning curve is used. This curve shows how model accuracy changes as the training set size increases. To plot this curve, the model is trained on datasets of various sizes.

4. PROPOSED FLOWCHART FOR ACCURATE AND FAST DETECTION OF THE RESONANCE PHENOMENON IN ACTIVE DISTRIBUTION NETWORKS

In this section, a workflow is proposed for employing the Genetic Algorithm (GA) to improve the accuracy and speed of LSTM performance in the process of classifying and distinguishing between the resonance phenomenon and other transient events in active distribution networks such as load changes, capacitor bank switching, etc.

As mentioned in the previous sections, one of the important applications of LSTM is classification based on time-series data. In this research, the detail and approximation coefficients of the DWT of the active distribution network voltage wave up to six levels during various transient events are used to produce time-series input features for LSTM training. To study various transient events, the test active distribution network, including distributed generation sources such as wind turbines, photovoltaics, and diesel generators, is first created in the PSCAD software. Then, to form a database of transient events such as single-phase, two-phase, and three-phase outages in the photovoltaic feeder, capacitor bank switching in the wind turbine feeder, and three-phase and two-phase load switching, are created. During a specific transient event, six detail coefficients for each phase voltage of the distribution network, i.e., 18 time-series features, are applied as training inputs to the LSTM. It should be noted that the size of the input vectors with time series for forming the training database is often different based on the type and time of the event. Here, the maximum number of hidden layers with full connectivity is considered equal to 50, and the factor that determines the minimum size of input data packets is considered equal to 1001. The number of learning epochs or, in other words, the Epoch factor (one round trip of input in the entire neural network) is completely optional, but it should be noted that determining more epochs leads to higher accuracy in the output and increases the learning time. On the other hand, if the number of learning epochs is too high, it may be difficult for LSTM to digest, or in other words, the network becomes "over-fit", therefore, the maximum number of Epochs is considered to be 15. Moreover, it is assumed that the detail coefficients up to the sixth level of the active distribution network voltage wave either indicate a resonance event or indicate other probable events such as capacitor bank switching, load switching, etc. Considering that the learning rate is set at 0.001, the number of 18 input features for 10 different transient events of phase cut, capacitor bank switching, and load during the training phase was used according to the assumed parameters, which after a period of 29 seconds during 15 iterations, the LSTM neural network finally reaches an accuracy of 85% in classifying transient events in the active distribution network. Since the main goal in this research is to use the genetic algorithm to improve the accuracy and speed of classifying the resonance event from other transient events in the active distribution network by LSTM, therefore, the fitness function of the genetic algorithm is defined according to equation (19).

$$fitness_{GA}^{LSTM} = \frac{(W_{Acc} \times LSTM_{Accuracy}^{Training})}{1+(W_{rt} \times LSTM_{RunTime}^{Training})} \tag{19}$$

In this regard, the indices $LSTM_{Accuracy}^{Training}$ and $LSTM_{RunTime}^{Training}$ are defined for the LSTM accuracy and speed, respectively, and the weight coefficients correspond to their importance. Two important and influential parameters, namely the number of hidden layers (H) and the maximum number of learning epochs (E), as well as the weight coefficients corresponding to the importance of accuracy and speed of the LSTM neural network, are selected as the genes of the sample chromosome according to Table (1) for optimization by the genetic algorithm. To execute the optimization process, a desired number of initial population (P) of chromosomes is generated for the genes or independent variables of the problem. After running the LSTM according to the available database corresponding to 10 transient events of the active distribution network and determining the accuracy and time of the training phase based on the parameters of the desired chromosome, then its fitness is calculated according to equation (19). The chromosomes are sorted in descending order of fitness values to enter the mating pool for performing the crossover process between pairs of chromosomes. This step is performed with a probability of *Pc* for the fittest chromosome pairs of the initial population according to Table (2). A number of offspring chromosomes are created from the crossover of parent chromosomes. Then, the mutation process is applied with a probability of *Pm* for a part of the population of offspring chromosomes according to Table (3). Table (1): Structure of a sample chromosome for improving the accuracy and speed of resonance phenomenon detection in active distribution networks by LSTM.

Table 1: structure of a sample chromosome used to improve the accuracy and speed of resonance phenomenon detection in active distribution networks using LSTM neural networks.

W_{rt}	W_{Acc}	MaxEpoch	numHiddenUnits

Table 2: crossover process between parent chromosomes in the genetic algorithm.

W_{rt}	W_{Acc}	MaxEpoch	numHiddenUnits
W_{rt}"	W_{Acc}"	MaxEpoch"	numHiddenUnits"
⇩		⇩	
W_{rt}	W_{Acc}	MaxEpoch"	numHiddenUnits"
W_{rt}"	W_{Acc}"	MaxEpoch	numHiddenUnits

Table 3: mutation process for offspring chromosomes.

W_{rt}	W_{Acc}	MaxEpoch""	numHiddenUnits"
W_{rt}"	W_{Acc}"	MaxEpoch	numHiddenUnits

By applying the crossover process, a number of ($(P_C \times pop)$) child chromosomes are added to the parent chromosomes. Subsequently, by employing the mutation process, an additional number of $(P_m \times pop)$chromosomes are appended to the existing chromosomes. Next, based on fitness values, 100 chromosomes are selected from the current population of $(pop_{old} + (P_C \times pop_{old}) + (P_m \times pop_{old}))$chromosomes for the next iteration of the algorithm. The previous steps are then repeated until the algorithm converges, meaning it reaches the maximum number of iterations. Finally, the numerical values from the last iteration of the genetic algorithm for the weight coefficients corresponding to the importance of LSTM's accuracy and speed, as well as its tuning parameters—including the number of hidden layers and the maximum number of learning epochs—are identified as the optimal solution to the problem[13].

The proposed flowchart for improving the speed and accuracy of LSTM performance by utilizing a genetic algorithm for detecting the sub-resonance phenomenon in active distribution networks is presented in Figure 8.

Figure 8: Proposed Flowchart for Enhancing the Speed and Accuracy of the LSTM Neural Network in Identifying and Detecting the Sub-Resonance Phenomenon in Active Distribution Networks Using a Genetic Algorithm.

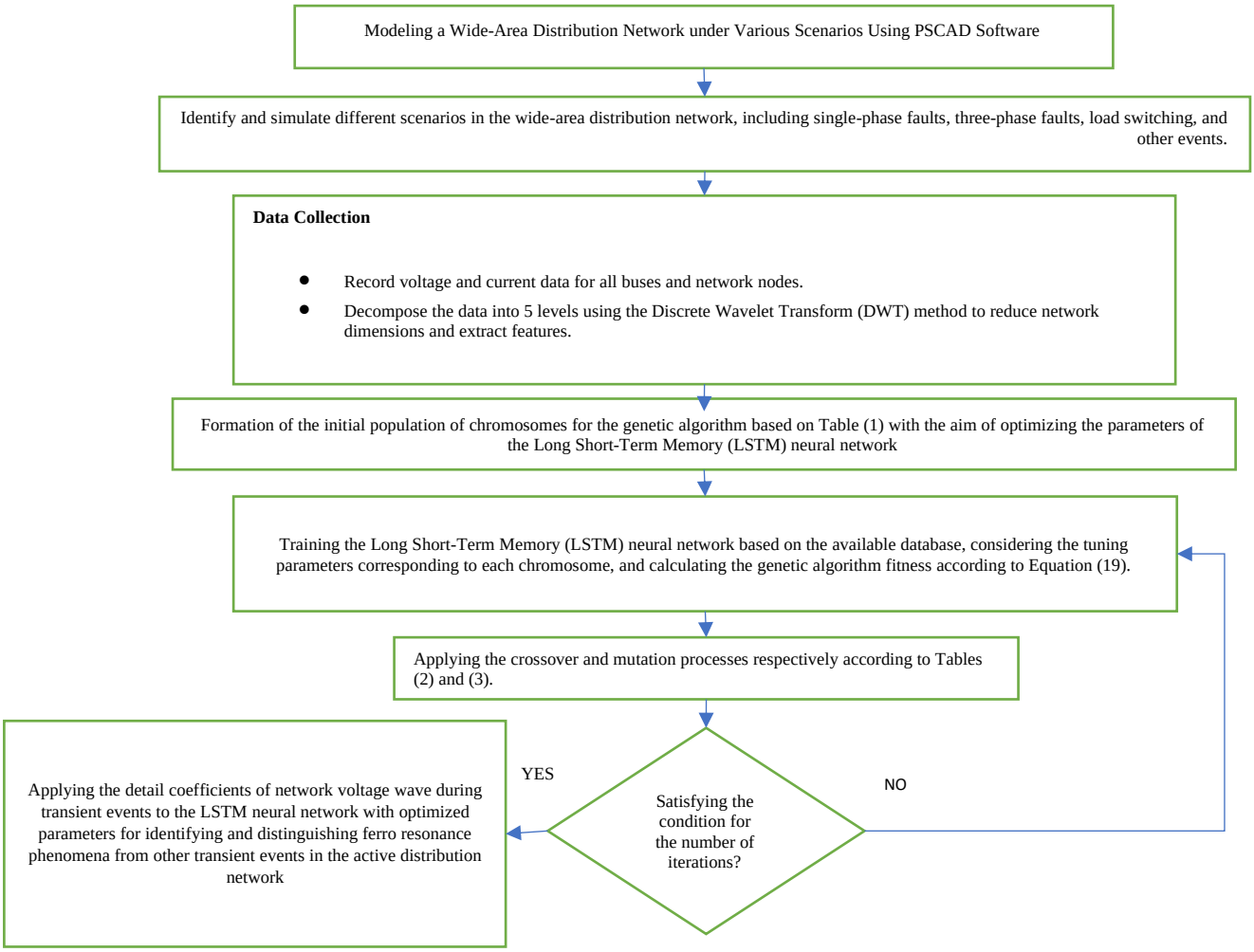

5.NUMERICAL STUDIES AND SIMULATION RESULTS

To validate and confirm the efficiency of the proposed algorithm in detecting the sub-resonance phenomenon, numerical studies are conducted on an active distribution network that includes distributed generation sources such as Photovoltaics (PVs), Wind Turbines (WTs), and standard Synchronous Diesel Generators (DGs). Various voltage wave signals are generated as a database for training the LSTM neural network by simulating normal operating conditions and the occurrence of transient events. These transient events include single-phase (a), two-phase (ab), and three-phase (abc) interruptions, capacitor bank switching, and load switching in the feeder connected to the Photovoltaic (PV) source, as well as capacitor bank switching in the feeder connected to the Synchronous Diesel Generator (DG). All simulations are performed using PSCAD software.

The single-line diagram of the studied active distribution network, created in the software, is shown in Figure 9. The upstream high-voltage network is connected to the medium-voltage distribution PCC bus through a 100 MVA transformer with a voltage ratio of 20 kV/63 kV. The primary and secondary connections of the transformer are configured in delta and star configurations, respectively. Figure 10 illustrates the schematic connection of the upstream network to the three main feeders (1, 2, and 3) of the distribution network. Measurement equipment is installed at the inputs of the main feeders to measure voltage magnitudes as well as the active and reactive power exchanges of the various existing distributed generation sources with the upstream grid.

Main Feeder Details:

- Feeder 1: Connected along the bus to a Wind Turbine (WT) with a nominal capacity of 10 MVA. It is linked to the distributed generation source via two 2.2-kilometer-long cable lines.

- Feeder 2: Connected along the bus to a Synchronous Diesel Generator (DG) with a nominal capacity of 0.3 MVA. It is connected to the distributed generation source through two 5-kilometer-long cable lines.
- Feeder 3: Connected along the bus to a Wind Turbine (WT) with a nominal capacity of 0.2 MVA. It is connected to the distributed generation source via two 2.2-kilometer-long cable lines.

The load demand along the three feeders is presented in Table 4.

Figure 5: Schematic of the Upstream Network and the Three Main Feeders of the Studied Distribution Network

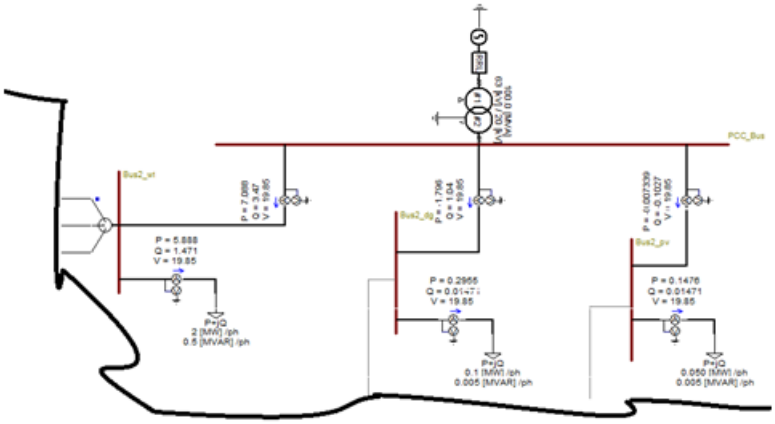

Table 4: Load Demand Along the Three Main Feeders of the Studied Active Distribution Network

Main Feeders	Load(Bus1)	Load(Bus2)
Feeder 1 (WT)	1(MW/ph) + j0.25(MVar/ph)	2(MW/ph) + j0.5(MVar/ph)
Feeder 2 (DG)	0.01(MW/ph) + j0.005(MVar/ph)	0.1(MW/ph) + j0.005(MVar/ph)
Feeder 3 (PV)	0.05(MW/ph) + j0.005(MVar/ph)	0.05(MW/ph) + j0.005(MVar/ph)

In Main Feeder 2, the DG distributed generation source supplies the equivalent local load of 1(MW/ph) + j0.005(MVar/ph). The WT source is connected to the end of Main Feeder 1 through a 20 MVA transformer with a voltage ratio of 6 kV / 20 kV and a star/star connection. The DG source is connected to the end of Main Feeder 2 through a 0.3 MVA transformer with a voltage ratio of 13.8 kV / 20 kV and a delta/star connection, while the PV source is connected to the end of Main Feeder 3 through a 0.2 MVA transformer with a voltage ratio of 0.6 kV / 20 kV and a delta/star connection. The average wind speed and solar irradiance in the area are 8 meters per second and 1400 watts per square meter, respectively.

The WT distributed generation source features three blades and a 50-meter-high tower and utilizes an induction generator with a squirrel cage winding to convert wind energy into electricity. The DG distributed generation source is equipped with a governor system and an Automatic Voltage Regulator (AVR). The PV distributed generation source consists of 22 series-connected modules in each array and 800 parallel modules in each array, with each module containing 36 series-connected solar cells. The output power of this source is injected into the feeder at a voltage level of 600 volts through an inverter using a boost converter.

A capacitor bank with a capacity of 10 microfarads is installed at the output of the PV distributed generation source's inverter under normal operating conditions on Main Feeder 3. Additionally, there are two switched capacitor banks in the network: one with a capacitance of 10 microfarads is placed in parallel with the active capacitor bank on Feeder 3, and another with a capacitance of 4 microfarads is located at the DG output. Three breakers are installed to disconnect the output phases of the PV source on Main Feeder 3. Furthermore, a switched load with active and reactive demands of [value missing] is located at Bus 1 of Main Feeder 3.

Since the primary objective of this research is to improve the speed and accuracy of detecting and identifying the sub-resonance phenomenon in the active distribution network using the hybrid LSTM-GA algorithm, numerical studies and simulations are conducted on the active distribution network built in PSCAD software under various normal and transient conditions as outlined below. This is done to create a temporally appropriate database and train the Long Short-Term Memory (LSTM) neural network for detecting the sub-resonance phenomenon and distinguishing it from other transient events.

Case Studies and Simulations

1. Case Study 1: Simulation of normal operating conditions of the active distribution network for a duration of 10 seconds.

2. Case Study 2: Simulation of a transient event involving the interruption of phase a for 6 seconds on Main Feeder 3.

3. Case Study 3: Simulation of a transient event involving the interruption of two phases, a and b, for 6 seconds on Main Feeder 3.

4. Case Study 4: Simulation of a transient event involving the interruption of three phases for 6 seconds on Main Feeder 3.

5. Case Study 5: Simulation of a transient event involving the switching of a 10 microfarad capacitor bank for 6.5 seconds on Main Feeder 3.

6. Case Study 6: Simulation of a transient event involving the switching of a 4 microfarad capacitor bank for 6.5 seconds on Main Feeder 2.

7. Case Study 7: Simulation of a transient event involving load switching starting at 6.75 seconds on Main Feeder 3.

8. Case Study 8: Simulation of a transient event involving a single-phase short circuit (phase A to ground) from 6.85 seconds to 10 seconds on Main Feeder 2.

9. Case Study 9: Simulation of a transient event involving a two-phase short circuit (phases A and B) to each other from 6.90 seconds to 10 seconds on Main Feeder 2.

10. Case Study 10: Simulation of a transient event involving a three-phase short circuit (phases A, B, and C) to each other and to the ground from 6.95 seconds to 10 seconds on Main Feeder 3.

After executing the simulations for these 10 case studies, the wavelet transform block is utilized to calculate the detail and approximation coefficients of the three-phase feeder voltage waveform at six levels under the transient events. The detail coefficients are then used as time-sequenced input features for the LSTM training phase.

Optimization with Genetic Algorithm

Since the speed and accuracy of sub-resonance detection and classification in the studied active distribution network by this neural network type are highly dependent on the number of hidden layers, the maximum number of learning epochs, and their corresponding weight coefficients, the determination and adjustment of the optimal values of these parameters are handled by the genetic algorithm, according to the proposed flowchart in Figure 8.

- Crossover Probability: 0.7
- Mutation Probability: 0.3
- Initial Population Size: 100 chromosomes
- Number of Iterations: 15 (as the convergence criterion)

The codes for the proposed LSTM-GA model are written in .m-file format in MATLAB. This software is installed on an ASUS laptop equipped with a 5-core 2 GHz processor and 2-terabyte secondary memory.

Subsequently, the simulation results for the case studies are presented sequentially. The LSTM neural network is trained twice: once with default parameters and once with the optimal parameters adjusted by the genetic algorithm.

The results obtained from these two methods are then tested and compared for detecting sub-resonance in the active distribution network against new transient events.

Case Study 1

A simulation of the normal operating conditions of the studied active distribution network was conducted for a duration of 10 seconds using PSCAD software. The simulation results for the power generated by the distributed generation sources—PV, WT, and DG—in the active distribution network under normal operating conditions are shown in Figure 11. It should be noted that the values displayed for the active and reactive power injected into Main Feeder 2 by the DG are after it has supplied its local load. The simulation results for the active and reactive power exchange between the upstream grid and the three main feeders (1, 2, and 3) are presented in Figure 12. The simulation results for the voltage levels of Main Feeders 1, 2, and 3 are shown in Figure 13. The simulation results indicate that the control systems of the DG and PV sources in Main Feeders 2 and 3, respectively, effectively regulate and maintain the terminal voltages at their set values. Additionally, the WT source transitions from motoring to generating mode within 4.5 seconds after startup, adjusts to the phase voltage, and maintains its level during normal operation over time.

Figure 6: Simulation Results for Power Generation by PV, WT, and DG Sources

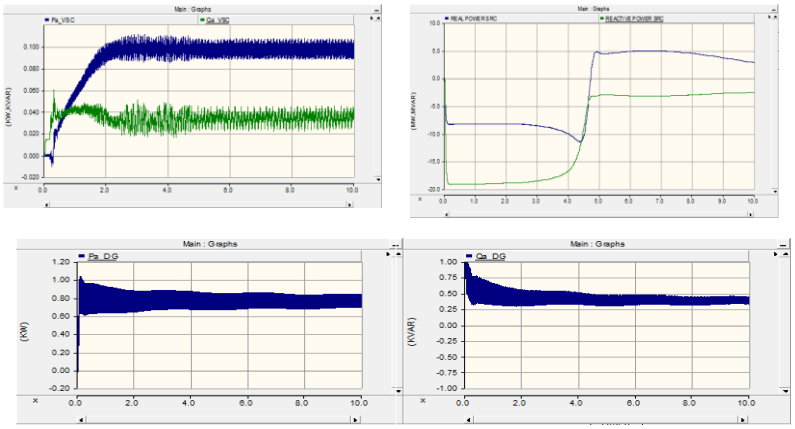

Figure 7: Active and Reactive Power Exchange of the Upstream Grid with Main Feeders 1, 2, and 3 of the Studied Active Distribution Network

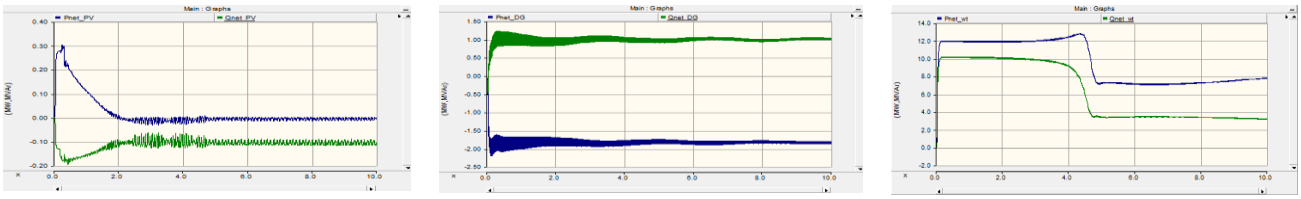

Figure 8: Voltage Levels at the Primary Side of the 0.2 MVA Transformer (0.6 kV/20 kV Delta/Star Connection) in Main Feeders 1, 2, and 3 of the Studied Active Distribution Network

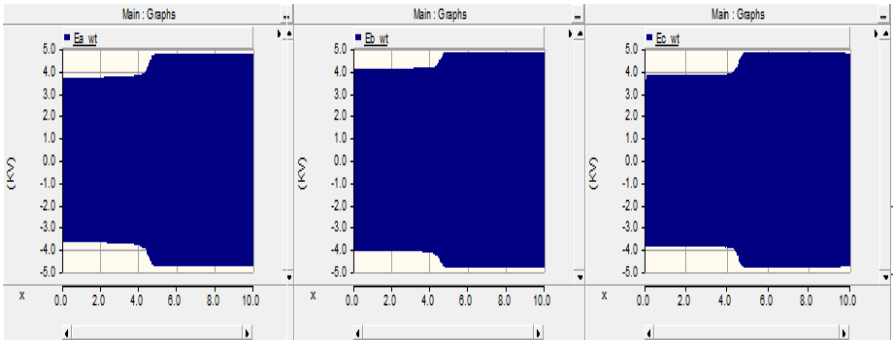

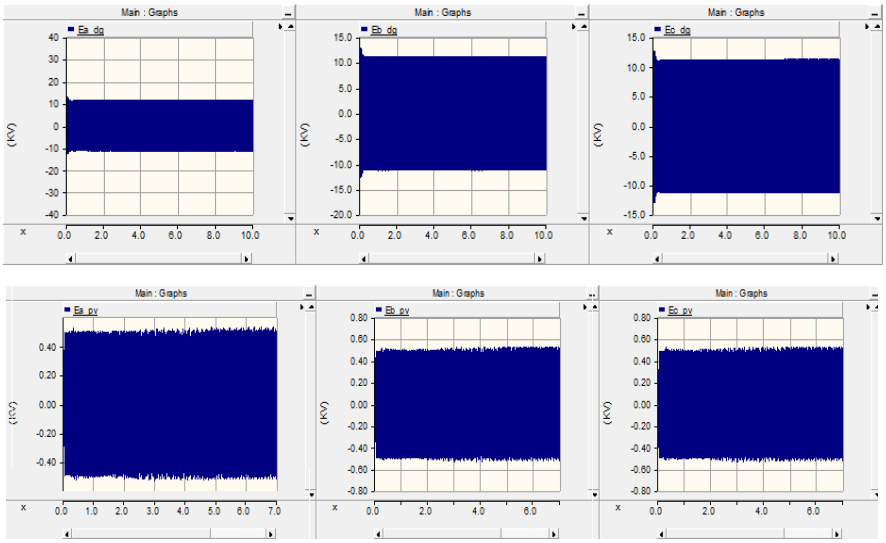

After applying the wavelet transform to the three-phase voltage waveforms of Main Feeders 1, 2, and 3, the feature extraction process for the training phase of the Long Short-Term Memory (LSTM) neural network follows. For example, the simulation results for the approximation coefficients and detail coefficients calculated for phases A, B, and C of the voltage waveform of Main Feeder 3 using the Discrete Wavelet Transform (DWT) over the time period from 0 to 0.2 seconds are presented in Figures 14 and 15.

Now, by applying wavelet transform to the three-phase voltage waveforms of the three main feeders 1, 2, and 3, the feature extraction process for the training phase of the Long Short-Term Memory (LSTM) neural network is followed. For example, the simulation results for the approximation coefficients (A) and detail coefficients (D) calculated for phases A, B, and C of the voltage waveform of main feeder 3 using Discrete Wavelet Transform (DWT) over the time period of 0 to 0.2 seconds are shown in Figures 9 and 10."

Figure 9: Approximation Coefficient for the Voltage Waveform of Main Feeder 3 under Normal Operating Conditions of the Distribution Network

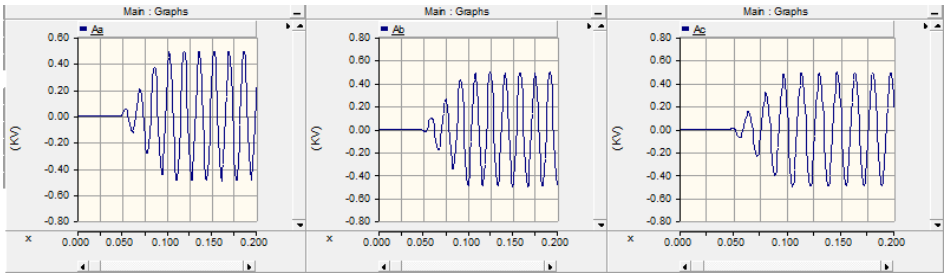

Figure 10: Detail Coefficients for the Three-Phase Voltage Waveform of Main Feeder 3 under Normal Operating Conditions of the Studied Distribution Network

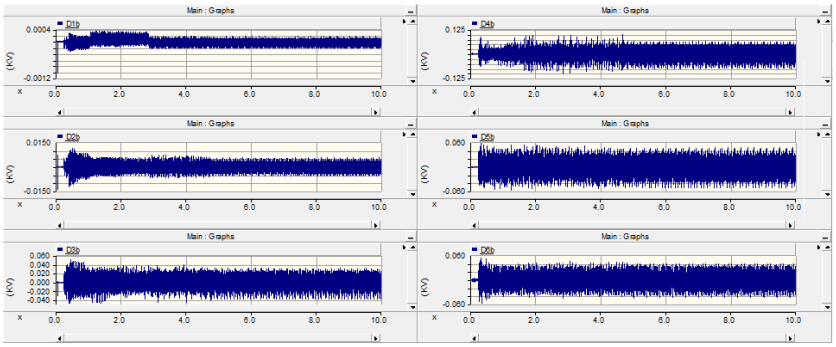

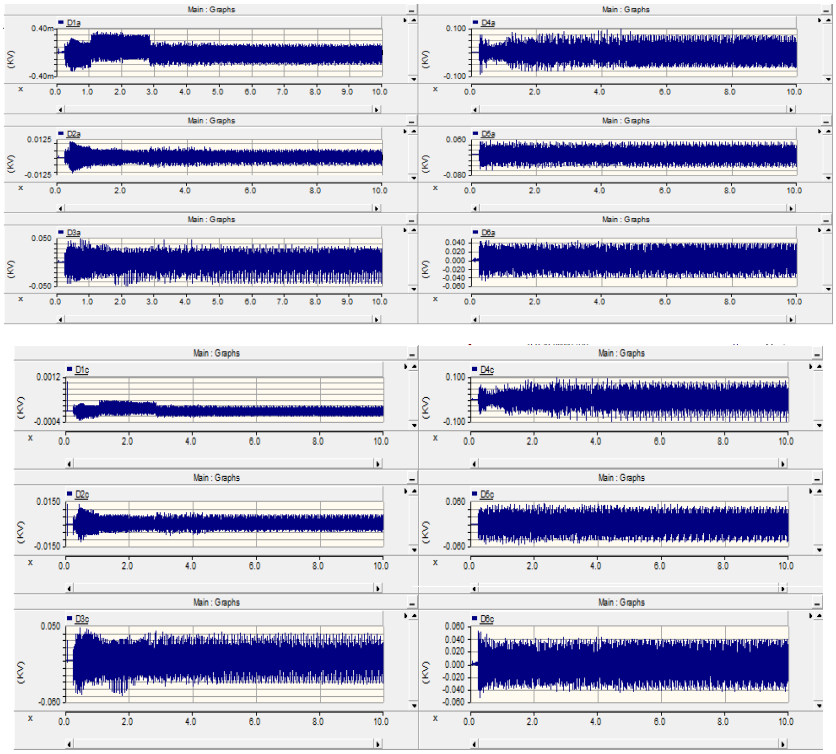

Case Study 2

A transient event simulation involving the interruption of phase a from 6 seconds to 10 seconds on Main Feeder 3 of the studied active distribution network was conducted using PSCAD software. The simulation results for the three-phase voltage waveform are shown in Figure 16. The simulation results indicate that the interruption of phase A in Main Feeder 3 disrupts the reactive power balance between the capacitive capacity of the lines, capacitor banks, and the linear and nonlinear inductances present in the network (such as line inductors and transformers with saturable cores). This imbalance leads to the sub-resonance phenomenon in the studied active distribution network. An overvoltage of up to three times the nominal value is caused by this phenomenon.

The approximation coefficients and detail coefficients calculated for phases A, B, and C of the voltage waveform of Main Feeder 3 using the Discrete Wavelet Transform (DWT) for use in the training phase of the LSTM network are presented in Figures 11 and 13.

Figure 11: Three-Phase Voltage Waveform During the Interruption of Phase a from 6 Seconds to 10 Seconds on Main Feeder 3 of the Studied Active Distribution Network

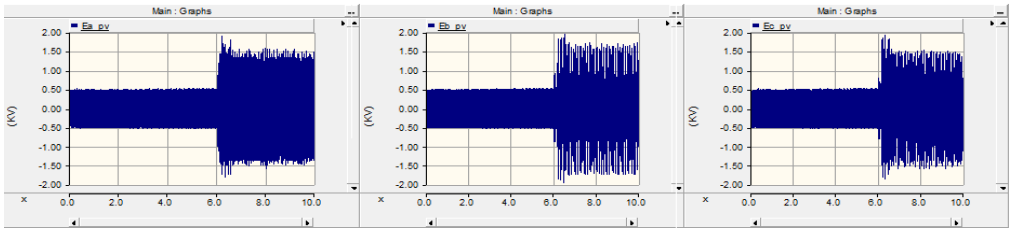

Figure 12: Simulation Results of the Approximation Coefficients for the Voltage Waveform Under Phase a Interruption Conditions from 6 Seconds to 10 Seconds on Main Feeder 3 of the Studied Active Distribution Network

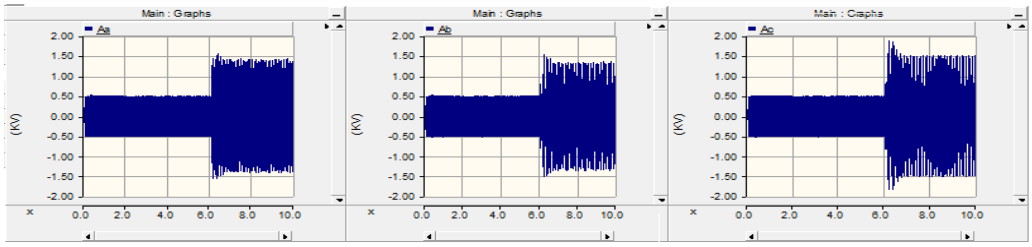

Figure 13: Simulation Results of the Detail Coefficients for the Voltage Waveform Under Phase a Interruption Conditions from 6 Seconds to 10 Seconds on Main Feeder 3 of the Studied Active Distribution Network

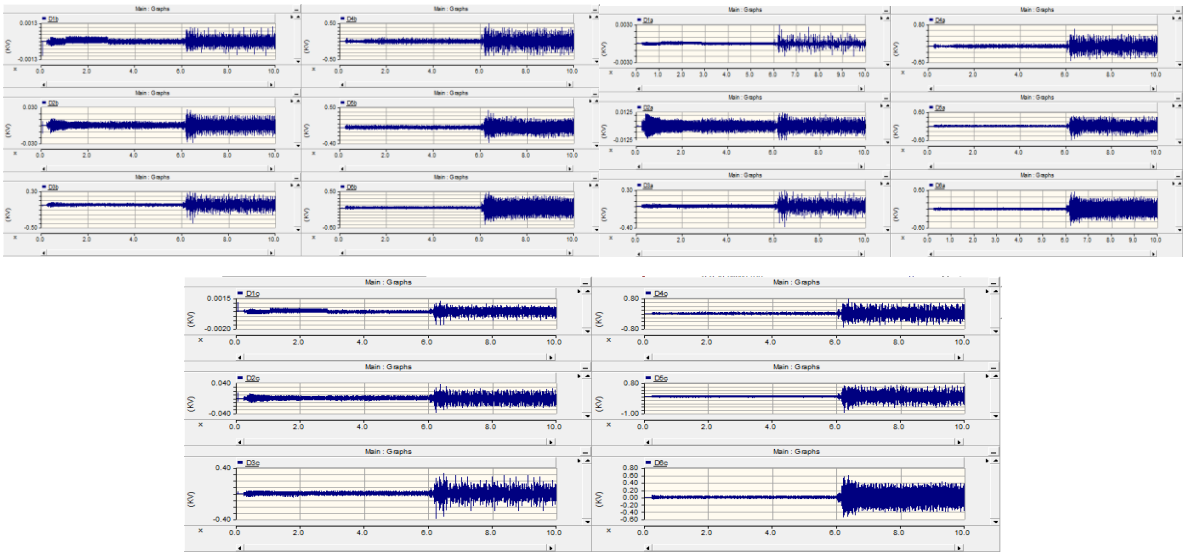

Case Study 3

A transient event simulation involving the interruption of phases a and b from 6 seconds to 10 seconds on Main Feeder 3 of the studied active distribution network was conducted using PSCAD software. The simulation results for the three-phase voltage waveform are shown in Figure 19. As seen in Figure 19, the interruption of phases a and b on Main Feeder 3 of the studied active distribution network from 6 seconds results in the occurrence of the sub-resonance phenomenon after the simulation is executed. This phenomenon causes an overvoltage imposed on phases a and b ranging from 4 to 5 times the normal value. The approximation coefficients and detail coefficients calculated for phases A, B, and C of the voltage waveform of Main Feeder 3 using the Discrete Wavelet Transform (DWT) are presented in Figures 14 and 16 for use in the training phase of the LSTM network.

Figure 14: Three-Phase Voltage Waveform During the Interruption of Phases a and b from 6 Seconds to 10 Seconds on Main Feeder 3 of the Studied Active Distribution Network

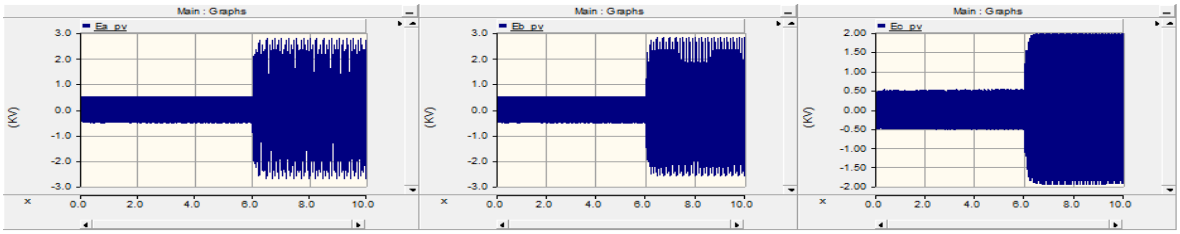

Figure 15: Simulation Results of the Approximation Coefficients for the Voltage Waveform Under Conditions of Phases a and b Interruption from 6 Seconds to 10 Seconds on Main Feeder 3 of the Studied Active Distribution Network

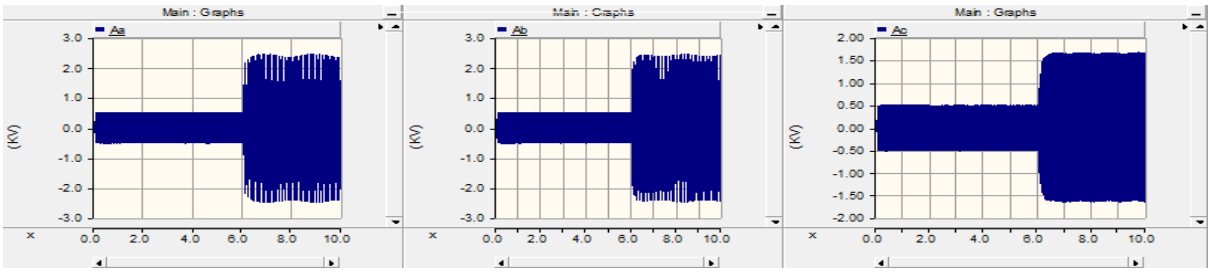

Figure 16: Simulation Results of the Detail Coefficients for the Voltage Waveform Under Conditions of Phases a and b Interruption from 6 Seconds to 10 Seconds on Main Feeder 3 of the Studied Active Distribution Network

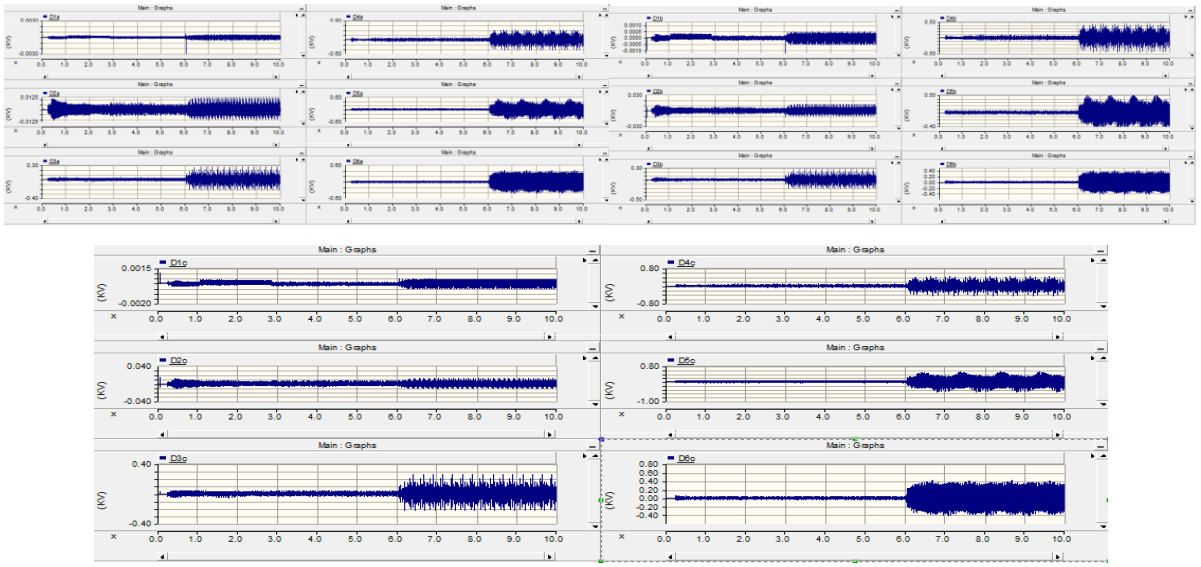

Case Study 4: A three-phase a, b, and c fault event is simulated from 6 to 10 seconds on the main feeder 3 of the active distribution network in PSCAD software. The simulation results for the three-phase voltage waveform are shown in Figure 22. As can be seen from the figure, the three-phase fault in the main feeder 3 does not result in a resonance phenomenon, and only a slight overvoltage is observed. The simulation results for the approximation coefficient (A) and detail coefficients (D) calculated for phases A, B, and C of the voltage waveform of main feeder 3 using Discrete Wavelet Transform (DWT) over the time period of 0 to 0.2 seconds are shown in Figures 17 and 19.

Figure 17: Three-phase voltage waveform during the three-phase a, b, and c fault event from 6 to 10 seconds on the main feeder 3 of the studied active distribution network.

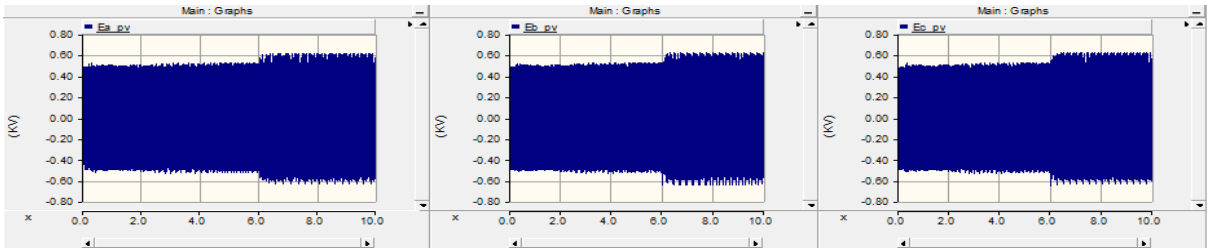

Figure 18: Simulation results of the approximation coefficient of the voltage waveform under the three-phase a, b, and c fault condition from 6 to 10 seconds on the main feeder 3 of the studied active distribution network.

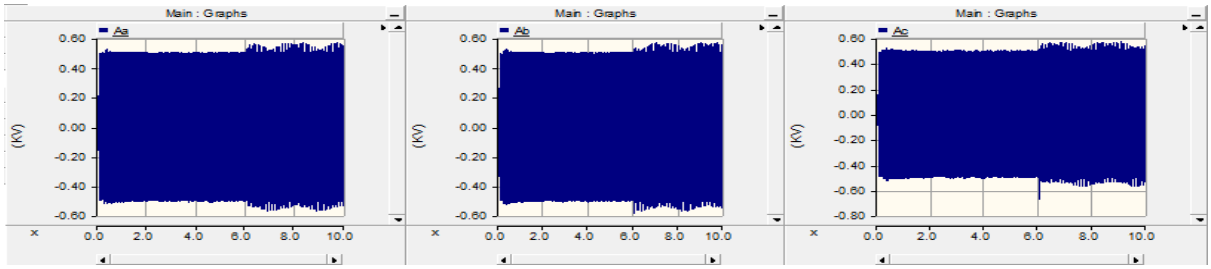

Figure 19: Simulation results of the detail coefficients of the voltage waveform under the three-phase a, b, and c fault condition from 6 to 10 seconds on the main feeder 3 of the studied active distribution network.

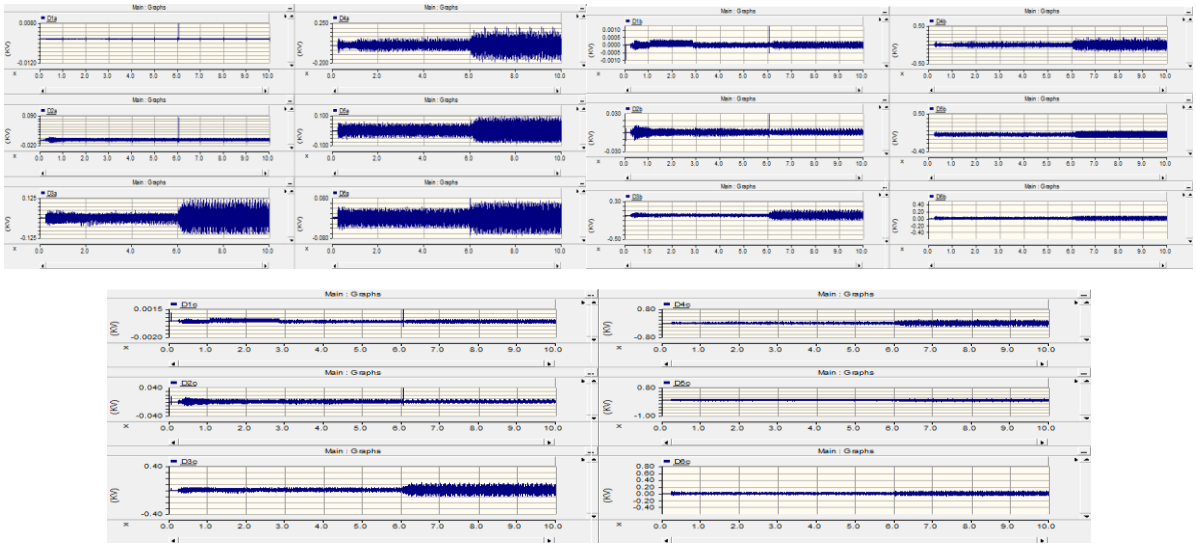

Case Study 5: A simulation of a 10 microfarad capacitor bank switching event at 6.5 seconds was conducted on main feeder 3 of the active distribution network using PSCAD software. The simulation results for the three-phase voltage waveform under the new conditions are shown in Figure 20. The results indicate that the switching of a 10-microfarad capacitor bank at 6.5 seconds on main feeder 3 of the studied active distribution network did not cause a significant change in voltage level and did not lead to the occurrence of resonance. The approximation coefficients (A) and detail coefficients (D) calculated for phases A, B, and C of the voltage waveform of main feeder 3 using Discrete Wavelet Transform (DWT) are shown in Figures 21 and 22.

Figure 20: Three-phase voltage waveform during the 10-microfarad capacitor bank switching event at 6.5 seconds on main feeder 3 of the studied active distribution network.

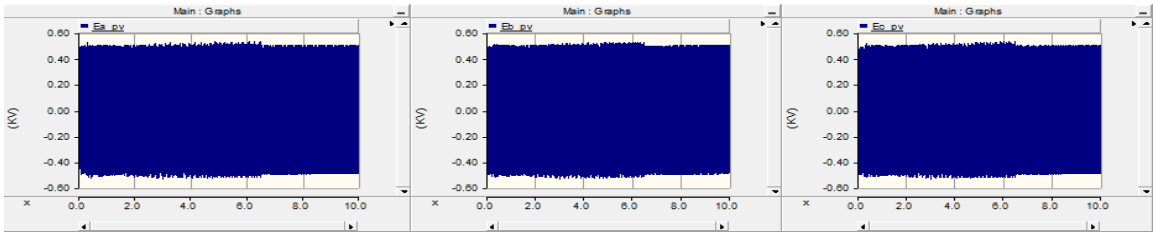

Figure 21: Simulation results of the approximation coefficient of the voltage waveform under the 10-microfarad capacitor bank switching condition at 6.5 seconds on main feeder 3 of the studied active distribution network. The lack of change in the approximation coefficients of phases A, B, and C in the above figures indicates that capacitor switching does not create conditions for the occurrence of resonance in the distribution network.

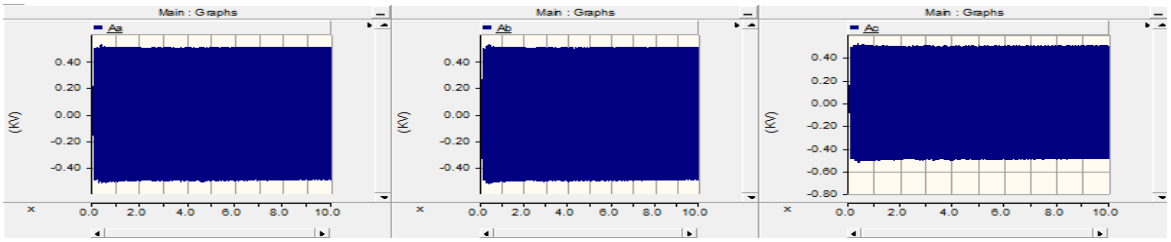

Figure 22: Simulation results of the detail coefficients of the voltage waveform under the 10-microfarad capacitor bank switching condition at 6.5 seconds on main feeder 3 of the studied active distribution network.

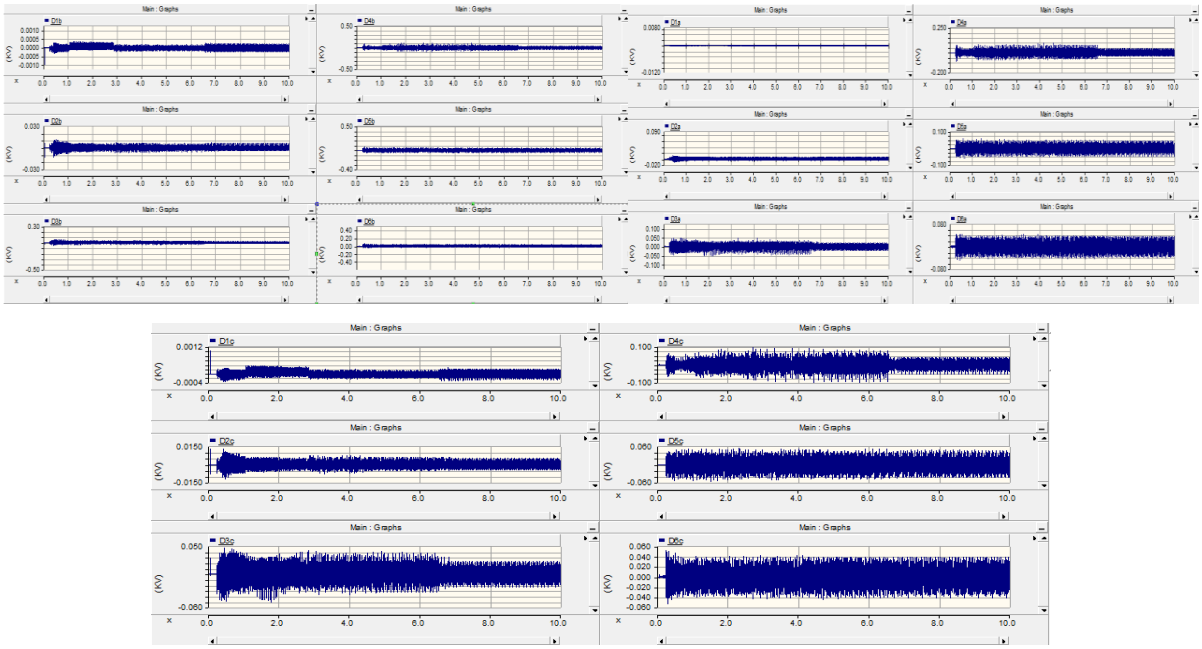

Case Study 6: A simulation of a 4-microfarad capacitor bank switching event, lasting for 0.25 seconds from 6.5 seconds, was conducted on main feeder 2 of the active distribution network using PSCAD software. The simulation results for the three-phase voltage waveform under these conditions are shown in Figure 28. The switching of the 4-microfarad capacitor bank at 6.5 seconds for 0.25 seconds on main feeder 2 of the studied active distribution network caused voltage fluctuations and a return to the initial value, but did not result in any significant overvoltage or resonance. The approximation coefficients (A) and detail coefficients (D) calculated for phases A, B, and C of the voltage waveform of main feeder 2 using Discrete Wavelet Transform (DWT) are shown in Figures 23 and 25.

Figure 23: Three-phase voltage waveform during the 4-microfarad capacitor bank switching event for 0.25 seconds starting at 6.5 seconds on main feeder 2 of the studied active distribution network.

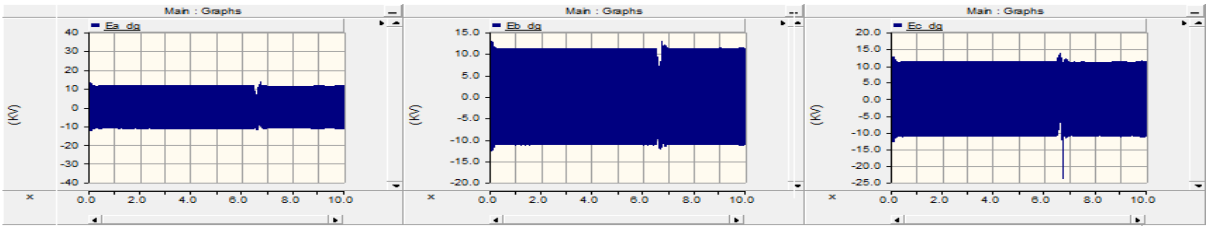

Figure 24: Simulation results for the approximation coefficient of the voltage waveform under the 4-microfarad capacitor bank switching condition at 6.5 seconds on main feeder 2 of the studied active distribution network.

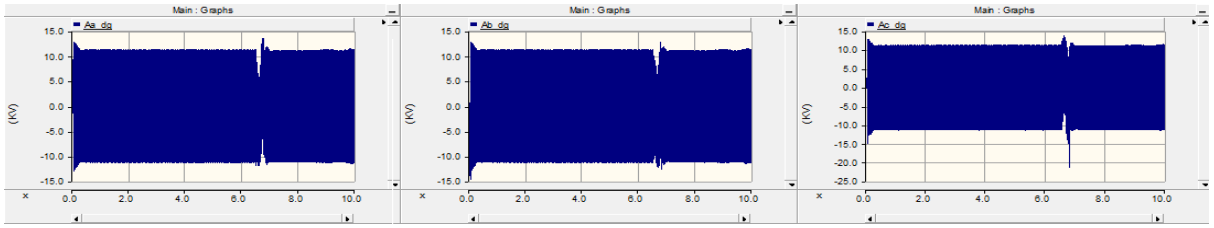

Figure 25: Simulation results of the detail coefficients of the voltage waveform under the 4-microfarad capacitor bank switching condition at 6.5 seconds on main feeder 2 of the studied active distribution network.

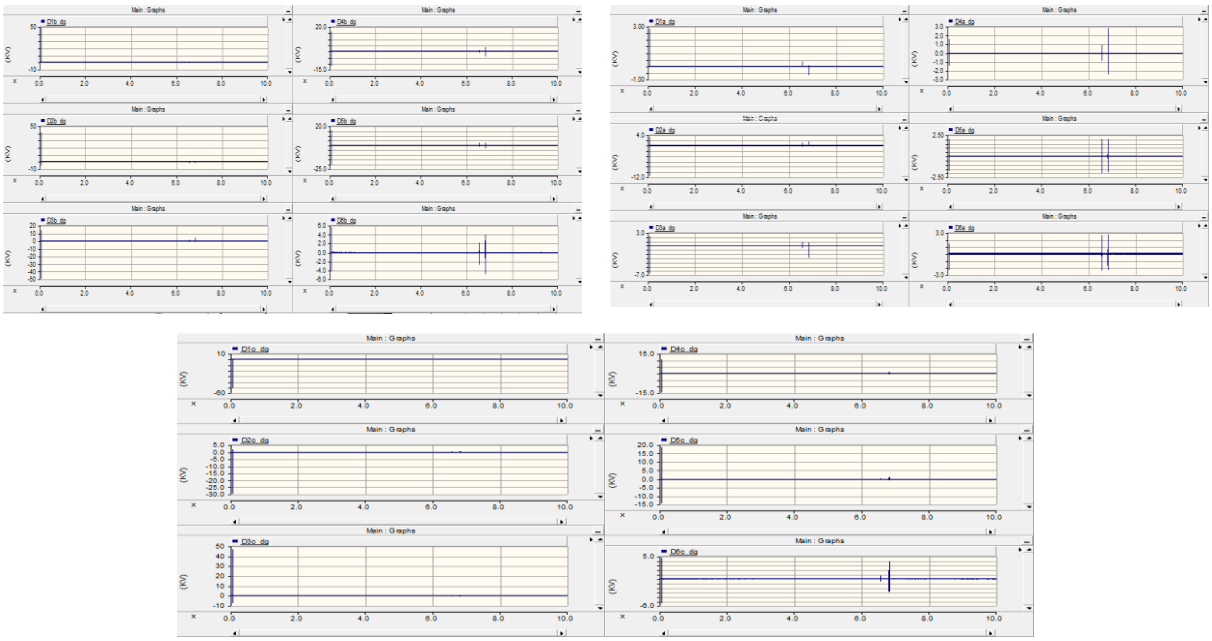

Case Study 7:A simulation of a load switching event at bus 1 of main feeder 3 from 6.75 seconds to 10 seconds was conducted on the active distribution network using PSCAD software. The simulation results for the three-phase voltage waveform under these new conditions are shown in Figure 31. Simulation results under the new load switching conditions at bus 1 of main feeder 3 from 6.75 seconds to 10 seconds were calculated. The approximation coefficient (A) and detail coefficients (D) calculated for phases A, B, and C of the voltage waveform using Discrete Wavelet Transform (DWT) are shown in Figures 26 and 28.

Figure 26: Three-phase voltage waveform during a load switching event at bus 1 of main feeder 3 from 6.75 seconds to 10 seconds on the studied active distribution network.

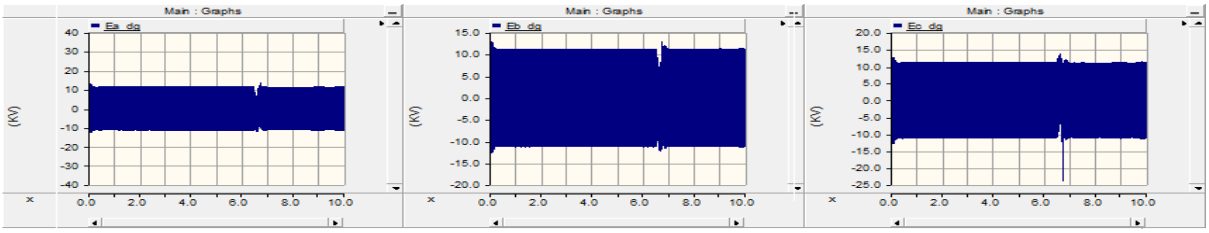

Figure 27: Simulation results of the approximation coefficient of the voltage waveform under load switching conditions at bus 1 of main feeder 3 from 6.75 seconds to 10 seconds for the studied active distribution network.

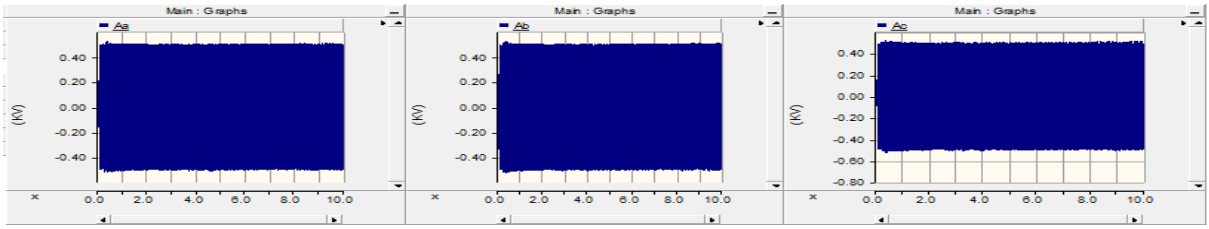

Figure 28: Simulation results of the detail coefficients of the voltage waveform under load switching conditions at bus 1 of main feeder 3 from 6.75 seconds to 10 seconds for the studied active distribution network.

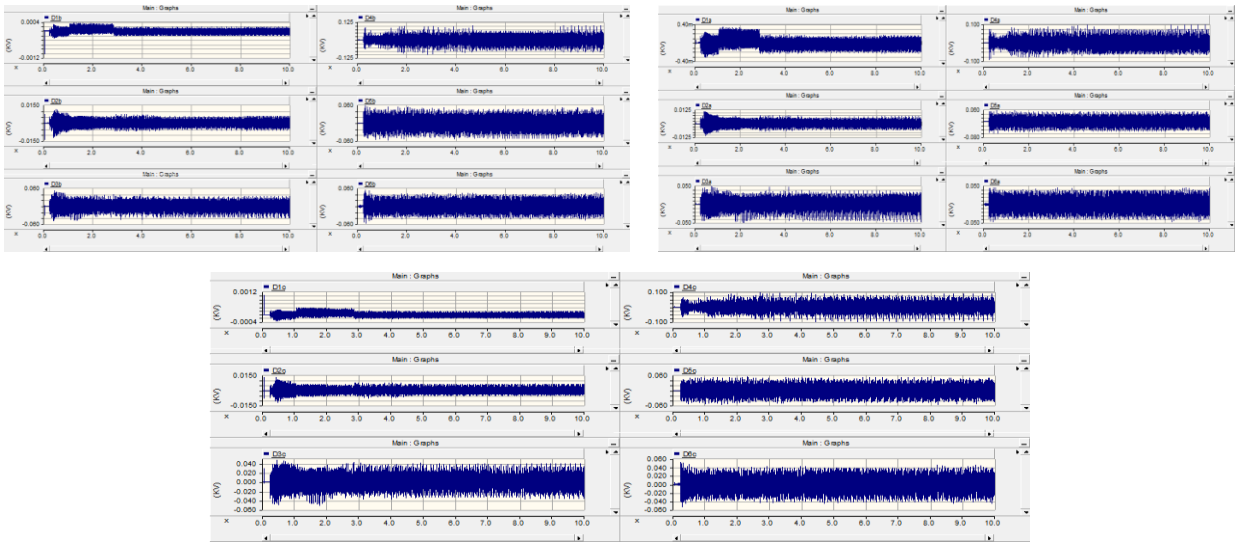

The simulation results indicate that the load switching on main feeder 3 did not induce any overvoltage in the network and did not cause a resonance phenomenon.

Case Study 8: A simulation of a single-phase A-to-ground fault from 6.85 to 10 seconds on main feeder 2 of the active distribution network was conducted in PSCAD software. The simulation results for the feeder 2 voltage are shown in Figure 35. The approximation coefficients (A) and detail coefficients (D) calculated for phases A, B, and C of the voltage waveform using Discrete Wavelet Transform (DWT) during the single-phase A-to-ground fault on main feeder 2 are shown in Figures 29 and 31.

Figure 29: Simulation results for the voltage level during a single-phase A-to-ground fault from 6.85 to 10 seconds on main feeder 2 of the studied active distribution network

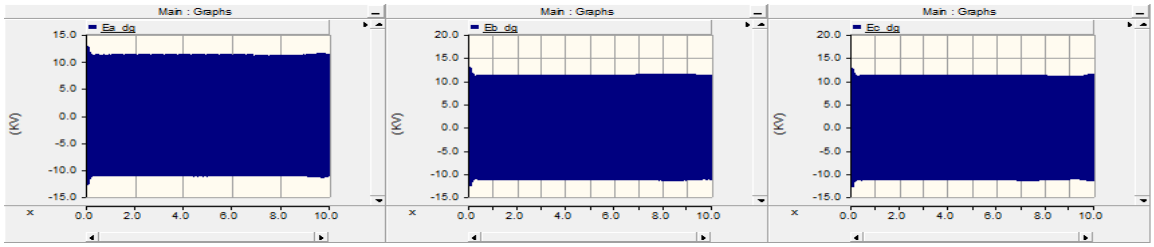

Figure 30: Simulation results of the approximation coefficient of the voltage waveform under a single-phase A-to-ground fault condition from 6.85 to 10 seconds on main feeder 2 of the studied active distribution network.

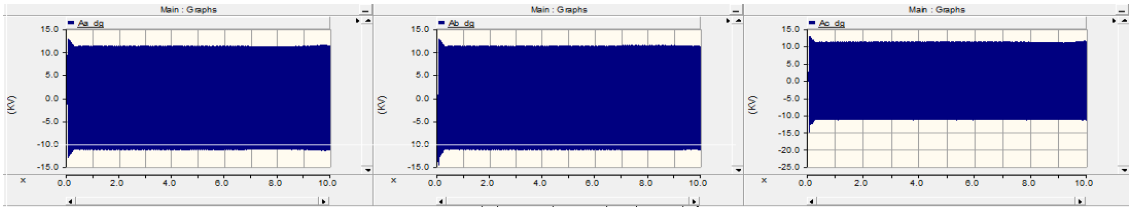

Figure 31: Simulation results of the detail coefficients of the voltage waveform under a single-phase A-to-ground fault condition from 6.85 to 10 seconds on main feeder 2 of the studied active distribution network.

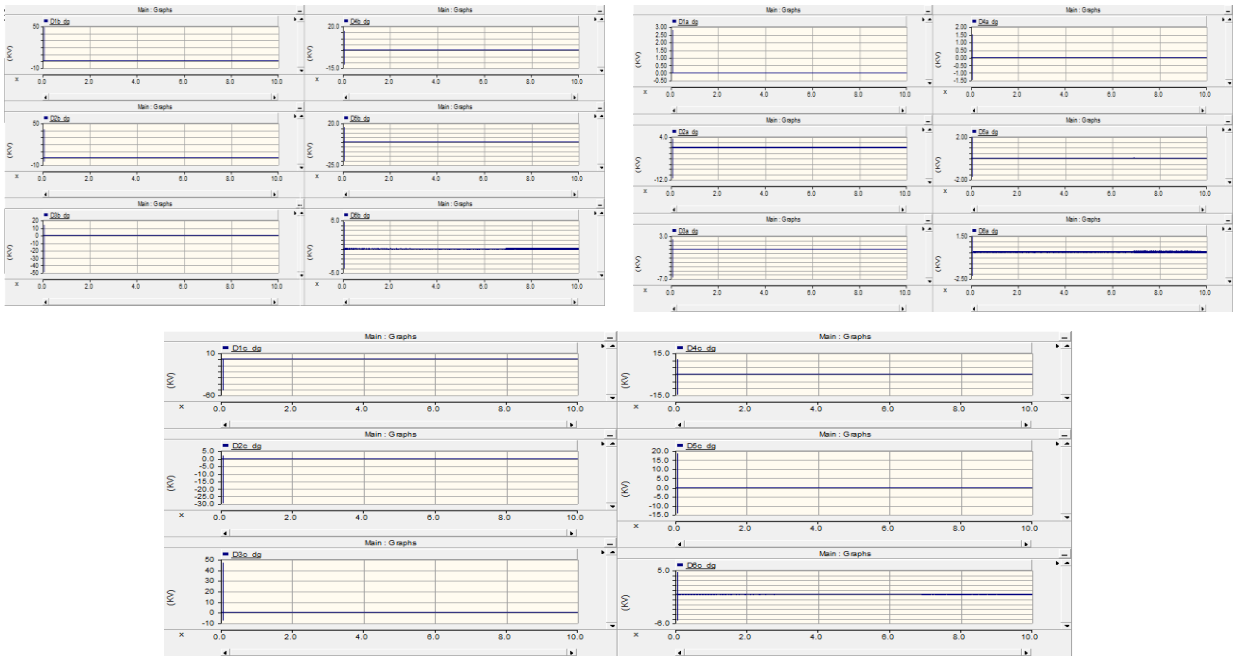

Case Study 9: A simulation of a two-phase A and B fault from 6.90 to 10 seconds on main feeder 3 of the studied active distribution network was conducted in PSCAD software. The simulation results for the feeder 3 voltage level are shown in Figure 38. The approximation coefficients (A) and detail coefficients (D) calculated for phases A, B, and C of the voltage waveform on feeder 3 using Discrete Wavelet Transform (DWT) are shown in Figures 32 and 34.

Figure 32: Simulation results for the voltage level during a two-phase A and B fault from 6.90 to 10 seconds on main feeder 3 of the studied active distribution network.

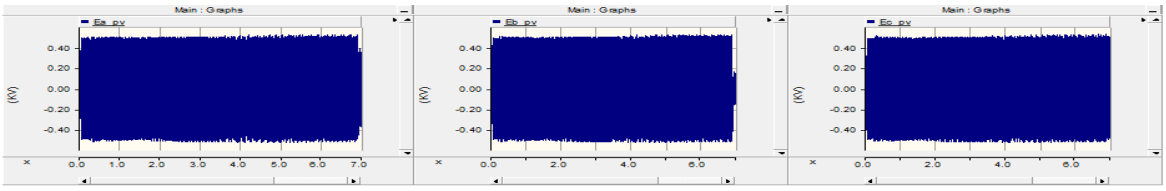

Figure 33: Simulation results of the approximation coefficient of the voltage waveform under a two-phase A and B fault condition from 6.90 to 10 seconds on main feeder 3 of the studied active distribution network.

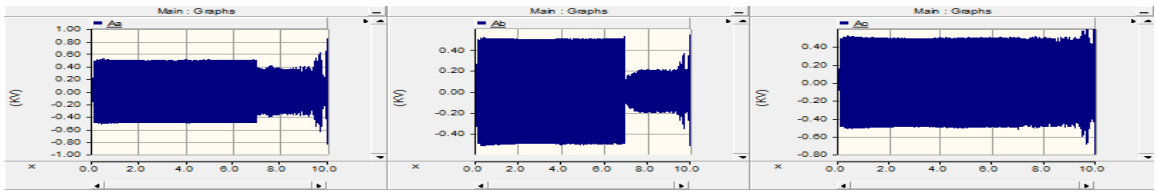

Figure 34: Simulation results of the detail coefficients of the voltage waveform under a two-phase A and B fault condition from 6.90 to 10 seconds on main feeder 3 of the studied active distribution network.

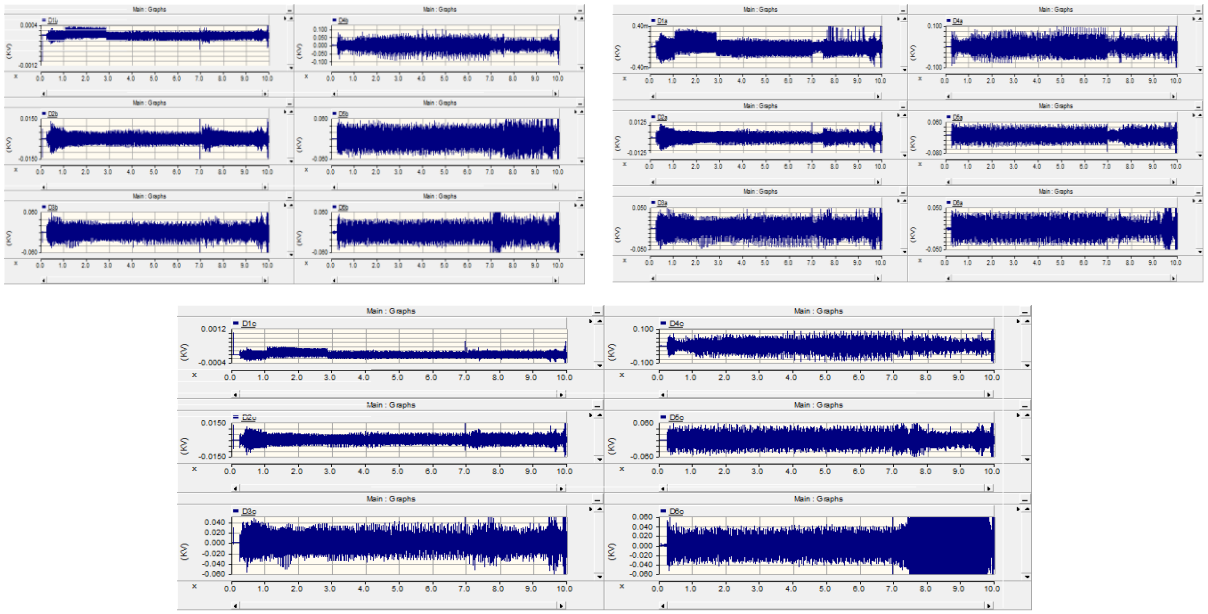

Case Study 10

A transient event simulation involving a three-phase short circuit to ground of phases A, B, and C from 6.95 seconds to 10 seconds on Main Feeder 3 of the studied active distribution network was conducted using PSCAD software. The simulation results under these conditions for the voltage level are shown in Figure 35.

Figure 35: Simulation Results of the Approximation Coefficient for the Voltage Waveform Under Three-Phase Short Circuit to Ground Conditions of Phases A, B, and C from 6.95 seconds to 10 seconds on Main Feeder 3 of the Studied Active Distribution Network

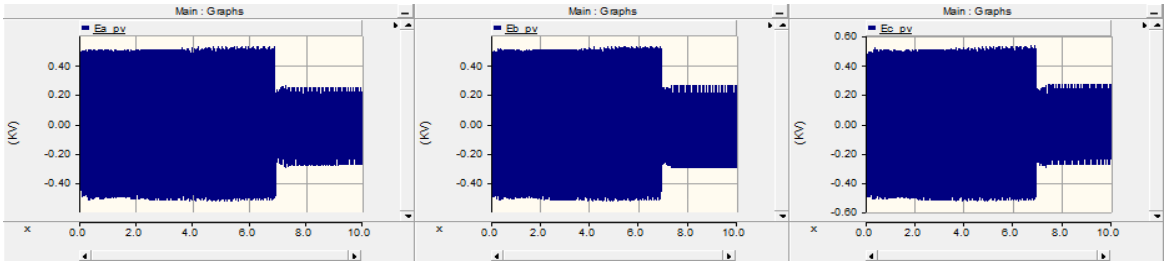

The approximation coefficients and detail coefficients calculated for phases A, B, and C of the voltage waveform using the Discrete Wavelet Transform (DWT) under three-phase short circuit to ground conditions are presented in Figures 36 and 37.

Figure 36: Simulation Results of the Approximation Coefficient for the Voltage Waveform Under Three-Phase Short Circuit to Ground Conditions of Phases A, B, and C from 6.95 seconds to 10 seconds on Main Feeder 3 of the Studied Active Distribution Network

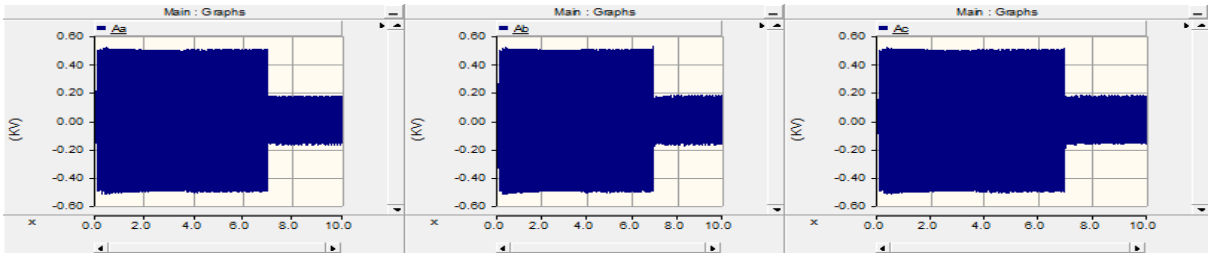

Figure 37: Simulation Results of the Detail Coefficients for the Voltage Waveform Under Three-Phase Short Circuit to Ground Conditions of Phases A, B, and C from 6.95 seconds to 10 seconds on Main Feeder 3 of the Studied Active Distribution Network

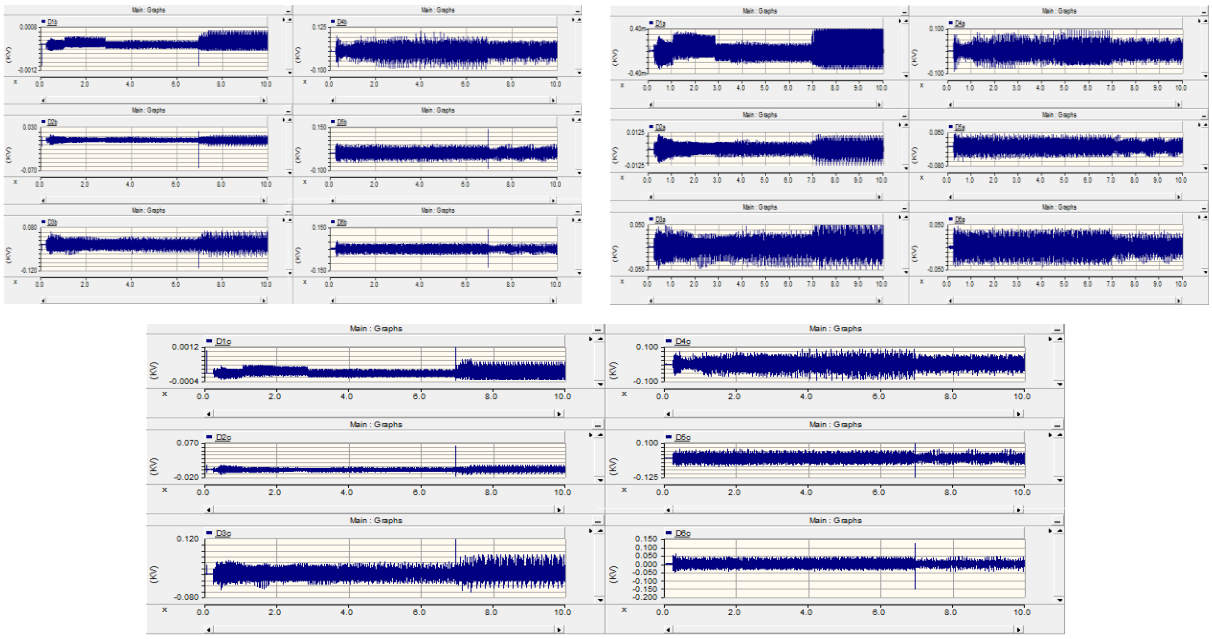

The simulation results indicate that the occurrence of a single-phase short circuit on Feeder 2 and two-phase and three-phase short circuits to ground on Main Feeder 3 of the studied active distribution network do not lead to the occurrence of the sub-resonance phenomenon in the network.

Next, by calculating the detail coefficients and analyzing the outcomes of each transient event in the case studies according to Table 5, we proceed to train the LSTM neural network in two scenarios: with default parameters and with parameters optimized by the genetic algorithm. This aims to prepare the neural network for estimating and identifying the sub-resonance phenomenon based on the voltage waveform information received from the feeders.

Table 5: Transient Events in the Studied Active Distribution Network and the Network's Condition Afterwards

Case Study	Transient Event in the Studied Active Distribution Network	Post-Event Network Condition
Case Study 1	Normal Operation of the Active Distribution Network	Non-Sub-Resonant
Case Study 2	Phase a Interruption on Main Feeder 3 from 6 seconds	Sub-Resonant
Case Study 3	Interruption of Phases a and b on Main Feeder 3 from 6 seconds	Sub-Resonant
Case Study 4	Three-Phase Interruption on Main Feeder 3 from 6 seconds	Non-Sub-Resonant
Case Study 5	Switching of a 10 Mirofarad Capacitor Bank on Main Feeder 3 from 6.5 seconds	Non-Sub-Resonant
Case Study 6	Switching of a 4 Mirofarad Capacitor Bank on Main Feeder 2 from 6.5 seconds	Non-Sub-Resonant
Case Study 7	Transient Switching of Load on Main Feeder 3 from 6.75 seconds	Non-Sub-Resonant
Case Study 8	Single-Phase A to Ground Short Circuit on Main Feeder 2 from 6.85 seconds	Non-Sub-Resonant

Case Study 9	Two-Phase A and B Short Circuit on Main Feeder 2 from 6.90 seconds	Non-Sub-Resonant
Case Study 10	Three-Phase A, B, and C to Ground Short Circuit on Main Feeder 3 from 6.95 seconds	Non-Sub-Resonant

Initially, the LSTM neural network is trained using the detail coefficients of the voltage waveforms from feeders undergoing transient events as input data and the resulting resonant or non-resonant condition of the studied active distribution network due to these events as the known output. This training is performed with 5 hidden processing layers and a maximum learning epoch of 15, based on the assumed parameters. During the training process, the data are sorted according to the number of time sequence elements and then tested to determine the neural network's accuracy in estimating the network's sub-resonant condition. Figures 44 and 45 illustrate, respectively, the sorting of data based on the input time sequence elements and the convergence trend to an appropriate accuracy for predicting the sub-resonance phenomenon. As seen in Figure 45, with the assumed parameters, the training time is 37 seconds, while the LSTM neural network ultimately achieves an 85% accuracy in estimating the sub-resonance phenomenon in the studied active distribution network. Subsequently, the neural network is retrained using a genetic algorithm with optimized parameters for the hidden processing layers and the learning epoch. The results for the optimized parameters of the LSTM neural network are presented in Table 6. The simulation results for the convergence of the genetic algorithm and the LSTM neural network during the training phase to the final accuracy for estimating sub-resonance in the studied active distribution network are shown in Figures 38 and 39, respectively.

Figure 38: Sorting of Data Based on Input Time Sequence Elements

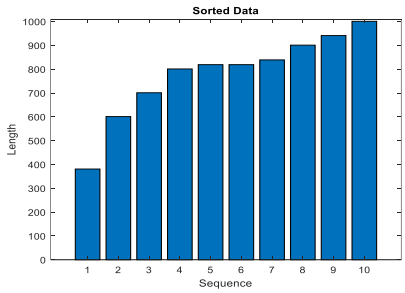

Figure 39: Convergence Trend to Suitable Accuracy for Predicting the Sub-Resonance Phenomenon

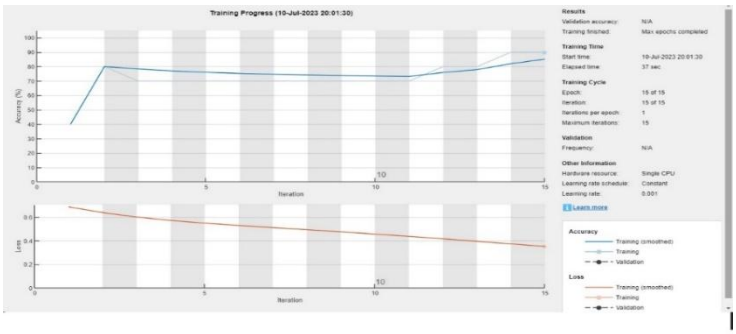

Table 6: Optimized Parameters for the LSTM Neural Network

W_{rt}	W_{Acc}	MaxEpoch	numHiddenUnits
0.3	0.7	20	41

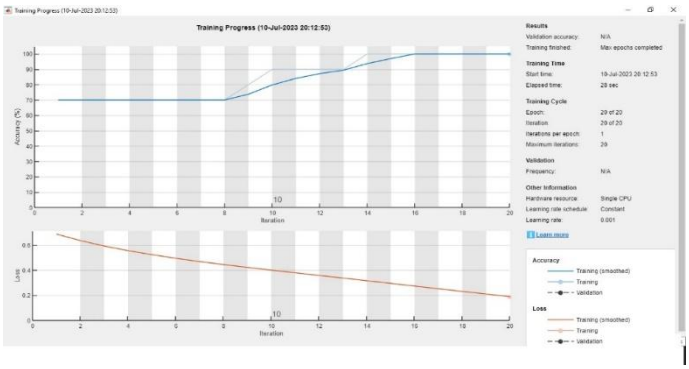

Figure 47: Simulation Results for the Convergence of the LSTM-GA Neural Network in the Training Phase to Final Accuracy for Estimating Sub-Resonance in the Active Distribution Network

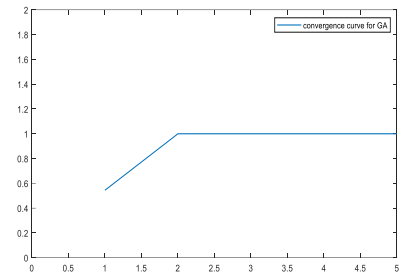

Figure 46: Simulation Results for the Convergence of the Genetic Algorithm in the LSTM Training Phase to Achieve Final Accuracy in Estimating Sub-Resonance in the Active Distribution Network

As can be seen from the figure, after 16 iterations in the training phase, 100% accuracy is achieved, and the time taken to reach this accuracy is 28 seconds. After completing the training and testing phase, the LSTM neural network with parameters optimized by the genetic algorithm is ready to predict the resonance phenomenon in the studied distribution network.

A total of 55 different transient events, including various types of short circuits (single-phase to ground, phase-to-phase, phase-to-phase to ground, and three-phase, totaling 10 events) at bus 1 of the three main feeders, phase outages (single-phase, two-phase, and three-phase on line 1 of the three main feeders, totaling 21 events), capacitor bank switching (at bus 2 of the three main feeders, totaling 3 events), and load switching (at bus 1 of the three main feeders, totaling 21 events) were arranged to evaluate and compare the performance of the LSTM and LSTM-GA neural network estimators.

When using the LSTM neural network estimator with default parameters, the true positive (TP) index is 5, the false positive (FP) index is 3, the true negative (TN) index is 42, and the false negative (FN) index is 3. However, when using the LSTM neural network estimator with parameters optimized by the genetic algorithm (GA), the true positive (TP) index is 7, the false positive (FP) index is 2, the true negative (TN) index is 43, and the false negative (FN) index is 1. The results are presented in terms of accuracy, precision, recall, and F1-score in Table 7.

Table 7 compares the performance indices for the LSTM and LSTM-GA neural networks for resonance phenomenon estimation. The simulation results in the table show that by optimizing the parameters of the number of hidden layers and the maximum learning epoch of the LSTM neural network using the genetic algorithm (GA), the performance indices, including accuracy by 10.4%, precision and recall by 15.2% and 25%, respectively, and F1-score by 19.8%, are improved.

Table 7: Comparison of Performance Indices for LSTM and LSTM-GA Neural Networks in Predicting the Sub-Resonance Phenomenon

Performance Index	*Accuracy*	*P*	*R*	*F1*
LSTM	86%	63%	63%	63%
LSTM-GA	91%	78%	88%	82%

The simulation results in the above table indicate that by optimizing the parameters of the number of hidden layers and the maximum learning epoch of the LSTM neural network, the performance indices increased by 10.4% in accuracy, 15.2% in precision, 25% in recall, and 19.8% in the F1 score.

6. Conclusion

In this article, the Genetic Algorithm (GA) is employed as a complementary method for optimizing the functional parameters of the Long Short-Term Memory (LSTM) neural network with the aim of improving classification accuracy and speed. The proposed hybrid framework is based on extracting feature information from the approximation coefficients and detail coefficients collected from the distribution network voltage waveforms.

To validate and confirm the effectiveness of the proposed model, numerical studies were conducted on an active distribution network that includes Distributed Generation sources such as Photovoltaics (PVs), Wind Turbines (WTs), and Distributed Generators (DGs). The studied active distribution network was constructed in the PSCAD software with assumed technical specifications, and a total of 10 case studies were utilized, including short-circuit events, capacitor bank switching, and load switching.

By employing the Discrete Wavelet Transform (DWT), the detail coefficients of the feeder voltage waveform during transient events were extracted and provided as input to the LSTM neural network for the training phase. Subsequently, the Genetic Algorithm was used to optimize the parameters of the number of hidden layers, the learning epoch of the algorithm, and their corresponding weight coefficients.

After completing the training and testing phases, the performance indices of the LSTM and LSTM-GA neural networks were compared. The simulation results confirm that by optimizing the parameters of the number of hidden layers and the maximum learning epoch of the LSTM neural network using the Genetic Algorithm (GA), the performance indices improved as follows:

- Accuracy: Increased by 10.4%
- Precision (P): Increased by 15.2%
- Recall (R): Increased by 25%
- F1 Score: Increased by 19.8%

These improvements highlight the effectiveness of the Genetic Algorithm in enhancing the predictive capabilities of the LSTM neural network for estimating the sub-resonance phenomenon in the studied active distribution network.

REFERENCES

[1] Mokryani, G., & Haghifam, M. 2008. Application of wavelet transform and MLP neural network for Ferroresonance identification. 2008 IEEE Power and Energy Society General Meeting - Conversion and Delivery of Electrical Energy in the 21st Century, 1-6.

[2] ElNozahy, M., El-Shatshat, R.A., & Salama, M. 2012. A robust technique for over-voltages classification in power transformers. 2012 IEEE Power and Energy Society General Meeting, 1-8.

[3] Sharbain, H.A., Osman, A., & El-Hag, A. 2017. Detection and identification of ferro-resonance. 2017 7th International Conference on Modeling, Simulation, and Applied Optimization (ICMSAO), 1-4.

[4] Mokryani, G., Haghifam, M.R., & Esmaeilpoor, J. 2007. Identification of ferro-resonance based on wavelet transform and artificial neural networks. 2007 Australasian Universities Power Engineering Conference, 1-6.

[5] Mokryani, G., Haghifam, M., Latafat, H., Aliparast, P., & Abdolahi, A. 2009. Wavelet Based Kernel Fisher Classifier for Ferro-resonance Identification. 2009 15th International Conference on Intelligent System Applications to Power Systems, 1-6.

[6] Mokryani, G., Siano, P., & Piccolo, A. 2010. Identification of ferroresonance based on S-transform and support vector machine. Simul. Model. Pract. Theory, 18, 1412-1424.

[7] Uzunoglu, C.P., & Ugur, M. 2013. Adaptive detection of chaotic oscillations in ferroresonance using modified extended Kalman filter. Turkish Journal of Electrical Engineering and Computer Sciences, 21, 1871-1879.

[8] Arroyo, A., Martinez, R., Manana, M., Pigazo, A., & Mínguez, R. 2019. Detection of ferroresonance occurrence in inductive voltage transformers through vibration analysis. International Journal of Electrical Power & Energy Systems, 106, 294-300.

[9] Chen, K., Hu, J., & He, J. 2018. A Framework for Automatically Extracting Overvoltage Features Based on Sparse Auto-encoder. IEEE Transactions on Smart Grid, 9, 594-604.

[10] Yang, M., Sima, W., Duan, P., Zou, M., Peng, D., Yang, Q., & Duan, Q. 2017a. Electromagnetic transient study on flexible control processes of ferro-resonance. International Journal of Electrical Power & Energy Systems, 93, 194-203.

[11] Nogay, H. S. 2023. Forecasting of voltage disturbances at the beginning of ferroresonance phenomena in power systems using by a new approach of long-short term memory (LSTM): LSTM for Ferroresonance in power systems. Journal of Engineering Research, 11, 1A, 1-15.

[12] Sadatian Moghaddam, P., Vaziri, A., & Ershadi Oskouei, A. (2024). A New Algorithm for Indoor Robot Localization using Turning Function. *Computational Methods for Differential Equations*.

[13] Vaziri, A., Sadatian Moghaddam, P., & Ershadi Oskouei, A. (2024). Development of service compositions in cloud manufacturing processes based on system sustainability components. *Journal of Electrical Systems, 19*(4), 418–434.